Article

Temperature, Doping, and Chemical Potential Tuning Intrinsic Defects Concentration in Bi₂MoO₆: GGA + *U* Method

Rui Wang, Liming Zhou,* and Wentao Wang*

ACCESS | Metrics & More | Article Recommendations | Supporting Information

ABSTRACT: Using the GGA + *U* method, the formation energy and concentration of intrinsic defects in Bi₂MoO₆ are explored under different chemical conditions, with/without doping, from 120 to 900 K. We find that the intrinsic defect and carrier concentration can be deduced from the small range of calculated Fermi levels in the diagram of formation energy vs Fermi level under different conditions. Once the doping conditions or/and temperature are determined, the corresponding E_F is only limited to a special region in the diagram of formation energy vs Fermi level, from which the magnitude relationship of defects concentration can be directly derived from their formation energy. The lower the defect formation energy is, the higher the defect concentration is. With E_F moving under different doping conditions, the intrinsic defect concentration changes accordingly.

At the same time, the highest electron concentration at the relative O-poor (point H_U) with only intrinsic defects confirms its intrinsic n-type behavior. Moreover, upon A⁻/D⁺ doping, E_F moves closer to VBM/CBM for the increasing concentration of holes/electrons. The electron concentration can also be further improved after D⁺ doping, indicating that D⁺ doping under O-poor chemical growth conditions is positive to improve its photogenerated carriers. This provides us with a method to adjust the intrinsic defect concentration and deepens our knowledge about comprehension and application of the diagram of formation energy vs Fermi level.
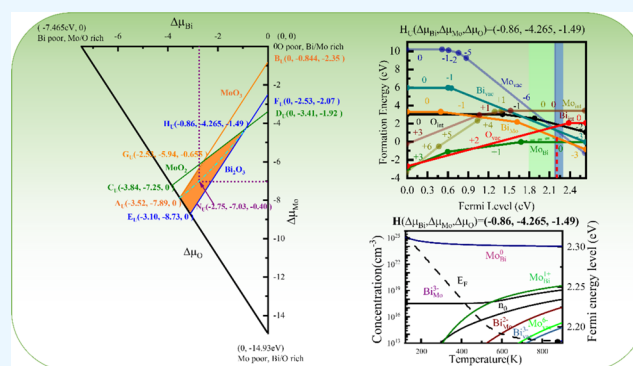
1. INTRODUCTION

Bi³⁺-based oxides such as Bi₂MoO₆, Bi₂WO₆, BiVO₄, and BiOCl are promising candidates for various applications, including solar cells, electrode materials, and photo-degradation of organic pollutants.[1−3] Bi₂MoO₆ is the most studied material in the photocatalytic field.[4] This is because Bi₂MoO₆ has good electron conductivity and visible-light response. The effective absorption of solar light is derived from the excellent electronic properties of Bi₂MoO₆ and the narrow band gap of 2.5−2.8 eV.[4] The density functional theory (DFT) calculations results show that the 2p electrons of O dominate its valance band; its conduction band consists predominantly of the 4d orbitals of Mo.[5] Nevertheless, pristine Bi₂MoO₆ has a poor production quantity of superoxide radicals under irradiation. Its little quadratic curvature of the conductive band bottom limits its practical application.[6−8] To improve the photocatalytic performance of pristine Bi₂MoO₆, considerable efforts have been conducted. For example, the morphology control of different dimensions, metal deposition, heterojunction fabrication, surface modification, and metal or nonmetal ion doping.[8,9]

Introducing intrinsic defects (such as O vacancy; Bi vacancy; Mo vacancy; Bi, Mo, O interstitial; Bi at Mo site and Mo at Bi site, and so on) into Bi₂MoO₆ is an efficient research method adopted to modify its photocatalytic efficiency.[10−16] Therefore,

the intrinsic defects of Bi₂MoO₆ have been widely explored. For example, Ding et al.[17] demonstrated that the self-doping of Bi in Bi₂MoO₆ can form Bi-substituted Mo (Bi_Mo) antisite and induce Mo vacancy. Using the Perdew−Burke−Ernzerhof (PBE) exchange-correction function calculations, they found that the electric charge around the substituted Bi atom for the Mo atom was redistributed. These defects cause a new band consisting of the O 2p orbital to appear in the unchanged band gap to favor its electron excitation. Di et al.[18] synthesized the Bi and O−Bi vacancy pairs in Bi₂MoO₆, displaying improved light absorption. Their DFT calculations observed that the increased density of states (DOS) at the valence band edge and new DOS appearing in the forbidden band improved the carrier concentration and made the excitation of electrons into the conduction band easier. Bi vacancy and Bi interstitial contained in Bi₂MoO₆ were synthesized by Zhang et al.[19] exhibiting higher photoexcitation.

Significantly, the single V_O defect in Bi_2MoO_6 is more importantly studied due to its relatively lower formational energy.[8,20] Huang et al.[21] synthesized different amounts of V_O in Bi_2MoO_6 with the higher tetracycline degradation rate of Bi_2MoO_6. Bai et al.[22] calcined Bi_2MoO_6 at 450 °C and found that it exhibited much higher photocatalytic performance owing to the existence of V_O. Yang et al.[23] experimentally achieved effective CO_2 photoconversion to CH_4 with high selectivity of up to 96.7% from well-designed V_O on Bi_2MoO_6. However, there is still a lack of quantitative description of native defects and carrier concentrations and their possible compensation relationship, which significantly impact the semiconductor catalytic properties in Bi_2MoO_6.

At the same time, theoretically, no research has been reported on the physics of all the intrinsic defects in Bi_2MoO_6, except a recent work by Jing et al.[24] They calculate the electronic structure and related properties of Bi_2MoO_6 with the native defects in a neutral state using standard DFT. However, the charged states are neglected. Honestly, the formation energy of a neutral impurity is independent of the Fermi level.[25,26] The Fermi level and, thus, the equilibrium concentration of the defects and carriers depend on chemical conditions such as temperature and the growth environment, which are not considered in previous research. Moreover, how intrinsic defects respond and compensate for the existence of extrinsically ionized impurities, such as donors and acceptors in Bi_2MoO_6, and how this relationship changes with temperature and chemical potentials has seldom been investigated. On the other hand, standard DFT calculation yield significantly underestimated band gaps, i.e., 1.76 eV,[24] compared to the experimental value of 2.46 eV.[27] Hence, more quantitatively, reliable calculations are required. The generalized gradient approximation (GGA) with on-site Coulomb interactions (GGA + U) within Dudarev's approach[28] is a reliable method for calculating defects' transition levels and formation energies,[29,30] which is implemented in this study.

In this work, we first investigated the formation energy of intrinsic defects and found the lowest energy of donors and acceptor forming Fermi pinning under different chemical potential conditions. Based on this, we then calculated the native defects and carrier concentration from 120 to 900 K and stated the relationship between defect concentration and their formation energies in the small zone of the calculated Fermi level. The highest electron concentration under relative O-poor conditions was found. Lastly, at the presence of A^- and D^+ doping under different chemical potential from 120 to 900 K, the concentrations of intrinsic defects and carriers were studied again, showing that D^+ doping under relative O-poor conditions can be further enhanced. We provide the first study of intrinsic concentration vs their formation energies within the special calculated Fermi level and promote the knowledge of comprehension and application of the diagram of formation energy vs Fermi level.

2. COMPUTATIONAL DETAILS

More details about DFT and formation energy calculation methods are shown in Note S1 (Supporting Information).

The lowest $E_f(X^q)$ part in the intersected plots of formation energy of different charged states of a certain defect can naturally form the trace of its formation energy. In this way, a defect constitutes a corresponding formation energy trace consisting of a series of polyline segments. When the traces of acceptors and donors with the lowest $E_f(X^q)$ intersect inside the band gap, the

Fermi level is pinned close to the intersection point. If the pinned E_F lies below the mid-gap, the system exhibits p-type behavior; otherwise, it is n-type.[31]

The defect formation energy is indeed a simple linear relationship between chemical potentials and the Fermi level as independent variables, at least if free carriers are ignored, a reasonable approximation if the Fermi level is far enough away from the valence-band edge.[32] The defect formation energy becomes a function of the Fermi energy solely, especially when the chemical potentials are fixed.[32] Actually, this formula (eq S1) and associated defect formation energy vs Fermi energy plot (Figure 2) are indeed commonly used to analyze, understand, and design the relevant properties of semiconductors without solving the detailed heat equations at a certain temperature. The Fermi-level pinning at the lowest crossing point of acceptor and donor formation energy vs Fermi energy lines at given atomic chemical potentials is often used as theoretical guidance for experiments to tune material performances by controlling growth conditions.[33]

Nevertheless, free carriers from thermal impurity levels and band-edge activations will always be present under certain doping concentrations at finite temperatures. Impurity excitation and intrinsic excitation will be further enhanced with the increasing temperature. This will affect the Fermi level position, especially when carrier concentrations are large compared to defect densities, which is usually crucial in semiconductors. In fact, the Fermi energy level is ultimately a function of chemical potentials and temperature when the doping concentration is determined. The following calculations of the self-consistent Fermi energy and the equilibrium defect and charge carrier concentrations took the influence of carriers into account.

In the synthesis process, the chemical potentials of Bi, Mo, and O in Bi_2MoO_6 are not arbitrary but subject to thermodynamic constraints, which can be used to represent actual experimental conditions. More details about the chemical potential calculation are shown in Note S2 (Supporting Information).

The phase diagram can be made when Bi_2MoO_6 exists stably. Equations S4−S7 defines the chemical potential in the tetrahedron with three vertices determined by $\Delta\mu_{Mo}$, $\Delta\mu_{Bi}$, and $\Delta\mu_O$, and the origin indicates that Mo, Bi, and O are all rich. For the sake of intuition, the tetrahedron is projected on the $\Delta\mu_{Mo}$, $\Delta\mu_{Bi}$ two-dimensional plane, and the projection is a triangle referring to Figure 1 for PBE + U calculations. For the triangle's apex, the origin (0, 0) means that both Bi and Mo are rich, $\Delta\mu_O = \Delta H_f(Bi_2MoO_6)/6 = -2.49$ eV; that is, O is poor. Point X (-7.465 eV, 0, 0) means Bi is poor and Mo/O is rich. Point Y (0, -14.93 eV, 0) means Mo is poor, and O/Bi is rich. The point on the hypotenuse XY means $\Delta\mu_O = 0$; that is, O is rich. Each line segment parallel to the hypotenuse represents that $\Delta\mu_O$ is equal to a constant, which keeps decreasing from the hypotenuse to the origin. Equations S1,S6−S8 limit the chemical potential stable region to be a trapezoid for GGA + U in the $\Delta\mu_{Bi}$ and $\Delta\mu_{Mo}$ plane,[34] as shown in Figure 1. We consider some representative points with coordinates ($\Delta\mu_{Bi}$, $\Delta\mu_{Mo}$, $\Delta\mu_O$) in units of eV, A_U (-3.52, -7.89, 0), G_U (-2.53, -5.94, -0.655), H_U (-0.86, -4.265, -1.49), E_U (-3.10, -8.73, 0), and N_U (-2.75, -7.03, -0.40) by PBE + U, respectively, also marked in the figure.

Comparing Figure 1 with the previous investigation,[24] we find that the PBE + U calculated stable region shaded for Bi_2MoO_6 is a smaller trapezoid than the irregular pentagon by PBE.
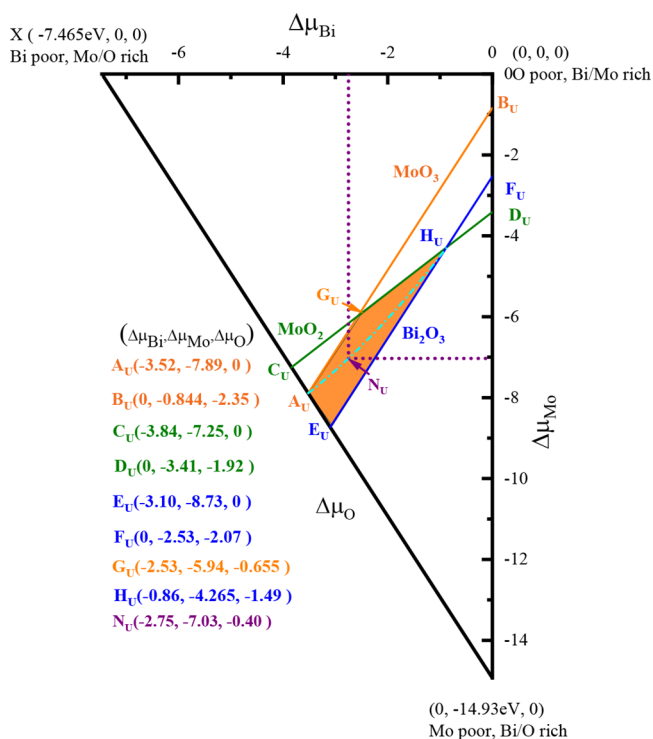
Figure 1. PBE + U calculates the accessible range of chemical potentials (orange region) for equilibrium growth conditions of orthorhombic Bi_2MoO_6. Specific points A_U, G_U, H_U, E_U, and N_U are chosen as the representative chemical potentials for the following defect formation energy calculation.

Specifically, $\Delta\mu_O$ and $\Delta\mu_{Mo}$ shrink greatly from $[0, -2.28]$ eV and $[-2.28, -8.84]$ eV to $[0, -1.49]$ eV and $[-4.625, -8.73]$ eV, respectively; however, $\Delta\mu_{Bi}$ shrinks slightly from $[0, -3.6]$ eV to $[-0.86, -3.52]$ eV, which mainly caused by the larger translational amount of the formation region of MoO_2 from Bi-poor and Mo-rich to Bi-rich and Mo-poor. It is shown that the influence on formation energy after adding U in transition metal in MoO_2 (heavier stoichiometric ratio of Mo) is much larger than that in MoO_3 (lighter stoichiometric ratio of Mo), so can it be seen in VO_2 and V_2O_5 between PBE and PBE + U.[35] The calculated defect formation energies of charged states depend on the selected values for $\mu_{Bi}(\Delta\mu_{Bi} + E_{Bi})$, $\mu_{Mo}(\Delta\mu_{Mo} + E_{Mo})$, $\mu_O(\Delta\mu_O + E_O)$, and the Fermi-level positions related to the corresponding chemical conditions, which need to meet the constraints to avoid the formation of the impurity-related competing phases.

3. RESULTS AND DISCUSSION

3.1. Formation Energy and Fermi-Level Pinning under Different Chemical Potentials.
We have systematically studied the following eight intrinsic defects in the Bi_2MoO_6 lattice: V_{Bi} (Bi vacancy), V_{Mo} (Mo vacancy), V_O (O vacancy), I_{Bi} (interstitial Bi), I_{Mo} (interstitial Mo), I_O (interstitial O), Bi_{Mo} (Bi replacing Mo), and Mo_{Bi} (Mo replacing Bi). The calculated lowest formation energies as a function of the Fermi level for each defect are shown under the different conditions of chemical potentials in Figure 2, in which all possible charge states of higher formation energy of the same defects are not shown for simplification. The formation energy of each charged defect state is lower than that of any other corresponding states shown in Figure 2 for the certain extension of the band gap from CBM

to VBM. We note that by fixing the chemical potentials from eq S1, the defect formation energy solely becomes a function of the Fermi energy without considering thermal activation, which acts as a reservoir for electrons.[32] The charged defects such as Mo_{Bi}, I_{Mo}, I_{Bi}, and V_O with positive and zero scopes are donors, while defects such as V_{Mo}, V_{Bi}, Bi_{Mo}, and I_O with negative and zero scopes are acceptors.

As shown in Figures 1 and 2, the chemical condition is represented by points A_U, E_U (Bi-poor, Mo-poor, and O-rich), N_U, G_U (moderate), and H_U (the maximum of μ_O to synthesize Bi_2MoO_6). At the chemical condition of A_U, N_U, G_U, and H_U, the Fermi level is pinned within the n-type conductive region. At point H_U, the Fermi level pinned the closest to CBM indicates the narrowest donor energy level and the highest concentration of its charge carriers because of the most easily thermal activation into the conduction bands.[31] However, at point E_U, the Fermi level is pinned to be at around 0.3 eV below the mid-gap showing p-type conductive behavior especially.

At O-rich A_U, the lowest-energy defect is V_{Mo}^{6-} for $E_F > 1.9$ eV. When thermal excitation is not considered, the Fermi energy level is pinned by the dominant native donors Mo+1 Bi and acceptors V_{Mo}^{3-} to be at ~1.3 eV below CBM. One would expect E_F to remain trapped roughly mid-gap, resulting in an intrinsically insulating material for intrinsic compensation.[36] From A_U to E_U shown in Figure 2a,b, with the chemical potential of Bi increasing and that of Mo decreasing, the formation energies of Mo_{Bi} and V_{Bi} are increased and the formation energy of the antisite defects Bi_{Mo} is decreased. In contrast, the formation energy of V_O is almost unchanged. Thus, the Fermi level is pinned most nearly at ~0.9 eV above VBM by Bi1− Mo and V_O^{2+} with the lowest formation energies, indicating n-type conductivity for the occurrence of the most typical self-compensation, which the present articles have never reported. Hence, under O-rich conditions (A_U and E_U), the Fermi pinning near mid-gap and self-compensation between donors and acceptors would limit its conductive behavior. This means that such extreme O-rich growth conditions should be avoided.

At moderate points N_U and G_U, the Fermi energy level is also pinned by Mo^{1+}_{Bi} and V_{Mo}^{3-} with Fermi-level pinning at the range of n-type conductivity. From N_U to G_U shown in Figure 2c,d, the chemical potentials of both Bi and Mo increased, and that of O decreased, so the formation energy of Mo_{Bi} gradually decreased and that of V_{Bi} slightly increased from eq S1. As a result, the position of Fermi pinning moved to CBM. From G_U to H_U (relative O-poor conditions) shown in Figure 2d,e, the chemical potentials of both Bi and Mo still increase and that of O greatly decrease. The formation energy of Bi_{Mo} decreased and that of V_{Bi} unceasingly increased; the Fermi energy level is pinned by Mo^{1+}_{Bi} and Bi^{3-}_{Mo} with the Fermi level pinning closer to CBM, indicating the best n-type conductive properties. Nevertheless, around Fermi pinning at points N_U, G_U, and H_U, the formation energy of the neutral state of Bi_{Mo} is even lower than the lowest formation energy donors and acceptors of Fermi pinning, suggesting that Bi^0_{Mo} is much easier to form.

3.2. Self-Consistent Fermi Energy, Equilibrium Carrier, and Defect Concentrations.
The Fermi energy is fixed by the charge-neutral condition rather than a free parameter.[32,33] From the computed defect formation energies and total density of states (TDOS) of Bi_2MoO_6, the computed self-consistent Fermi energy E_F and carrier concentrations (n_0 for electrons and p_0 for holes) and defect concentrations (denoted as[Xq defect]) as a function of temperature T from 20 to 900 K under different chemical potential conditions of A_U, H_U, N_U, G_U, and E_U are
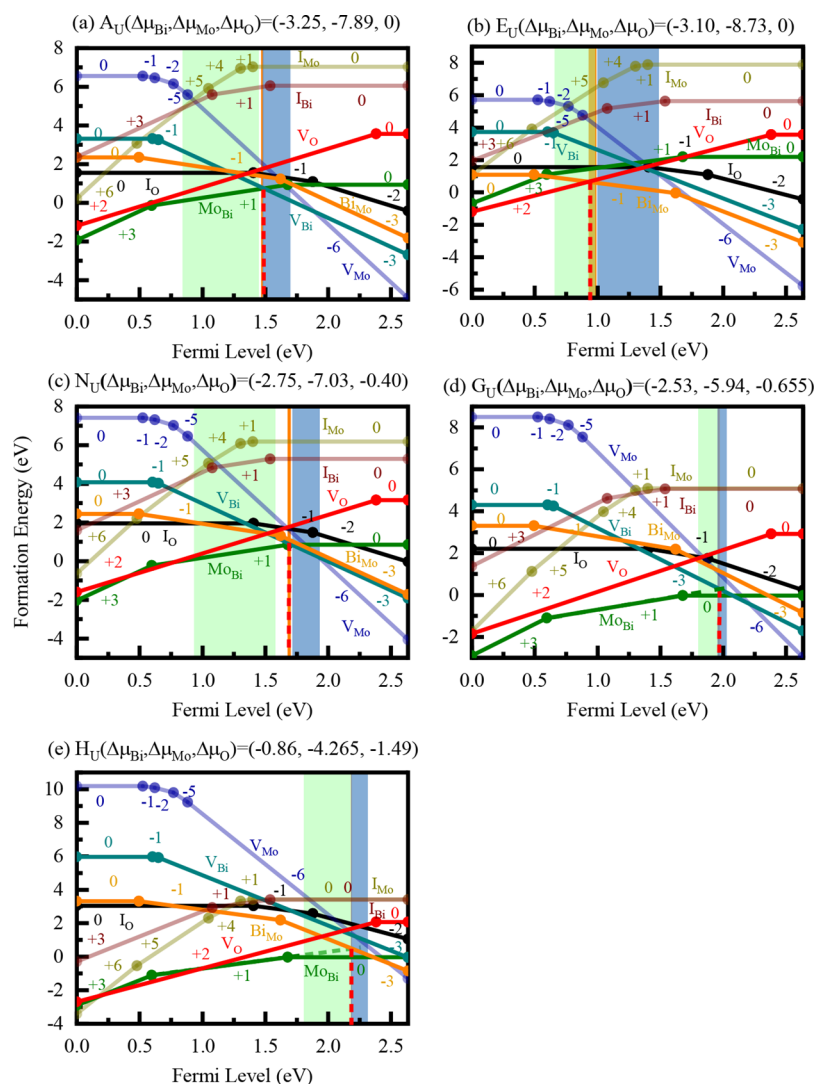
Figure 2. Formation energies (derived from PBE + U calculation) of intrinsic defects V_{Bi}, V_{Mo}, V_O, I_{Bi}, I_{Mo}, I_O, Mo_{Bi}, and Bi_{Mo} in Bi_2MoO_6 under different chemical potential conditions of (a) A_U, (b) E_U, (c) H_U, (d) G_U, and (e) N_U as shown, plotted as a function of the Fermi level with respect to the valence band maximum (VBM). Red dashed lines indicate each Fermi-level pinning. The Fermi level (E_F) at the VBM and CBM is set to 0.00 and 2.635 eV, respectively. The numbers in the polygonal lines denote the favorably charged states of each defect, in which different parallel line segments imply the same charge state, and so as in all the different chemical conditions. The orange, green, and blue areas represent the ranges of later calculated self-consistent Fermi levels with intrinsic defects, A^- doping, and D doping as a function of temperature T from 20 to 900 K under charge neutrality conditions, respectively, which can be seen in Table 1 for details.

shown in Figure 3. We calculate them using the code SC-FERMI with the dilute defect approximation. The defect formation energies, unit cell parameters, calculated total density of states in pristine crystal, and band gaps are assumed not to change with T for simplicity.[36,37]

At infinite temperature, the electrons (n_0) from CBM and holes (p_0) from VBM thermal excitations will always be present to affect the Fermi-level position, the concentrations of which are given by the following:[37]

$$n_0 = \int_{E_g}^{\infty} f_e(E)\rho(E)dE \tag{1}$$

$$p_0 = \int_{-\infty}^{0} f_h(E)\rho(E)dE \tag{2}$$

where E_g is the band gap, $f_e(E) = [\exp((E_F - E)/kT) + 1]^{-1}$ is the Fermi−Dirac distribution function, and $f_h(E)$ is defined as $1 - f_e(E)$ (k is the Boltzmann constant), $\rho(E)$ is the total density

of states (TDOSs) of the host cell without defects, and T is the temperature.

If the band gap (E_g) is taken into account with zero energy set at VBM, eq 1 can be written as follows:[33]

$$n_0 = N_c e^{-E_g - E_F/kT}, \quad N_c = \int_{E_g}^{\infty} dE[e^{-E_g - E_F/kT} + e^{E - E_g/kT}]^{-1}\rho(E) \tag{3}$$

$$p_0 = N_v e^{-E_F/kT}, \quad N_v = \int_{-\infty}^{0} dE[e^{-E_F/kT} + e^{-E/kT}]^{-1}\rho(E) \tag{4}$$

The concentration of the defect X with charged state q refers to

$$[C_X^q] = N_X g_{X^q} \exp\left(-\frac{E_f(X^q)}{kT}\right) \tag{5}$$

where N_X is the density of sites of the host cell where defects can form, g_{X^q} is the degeneracy of the defect state q, ($E_f(X^q)$) is the
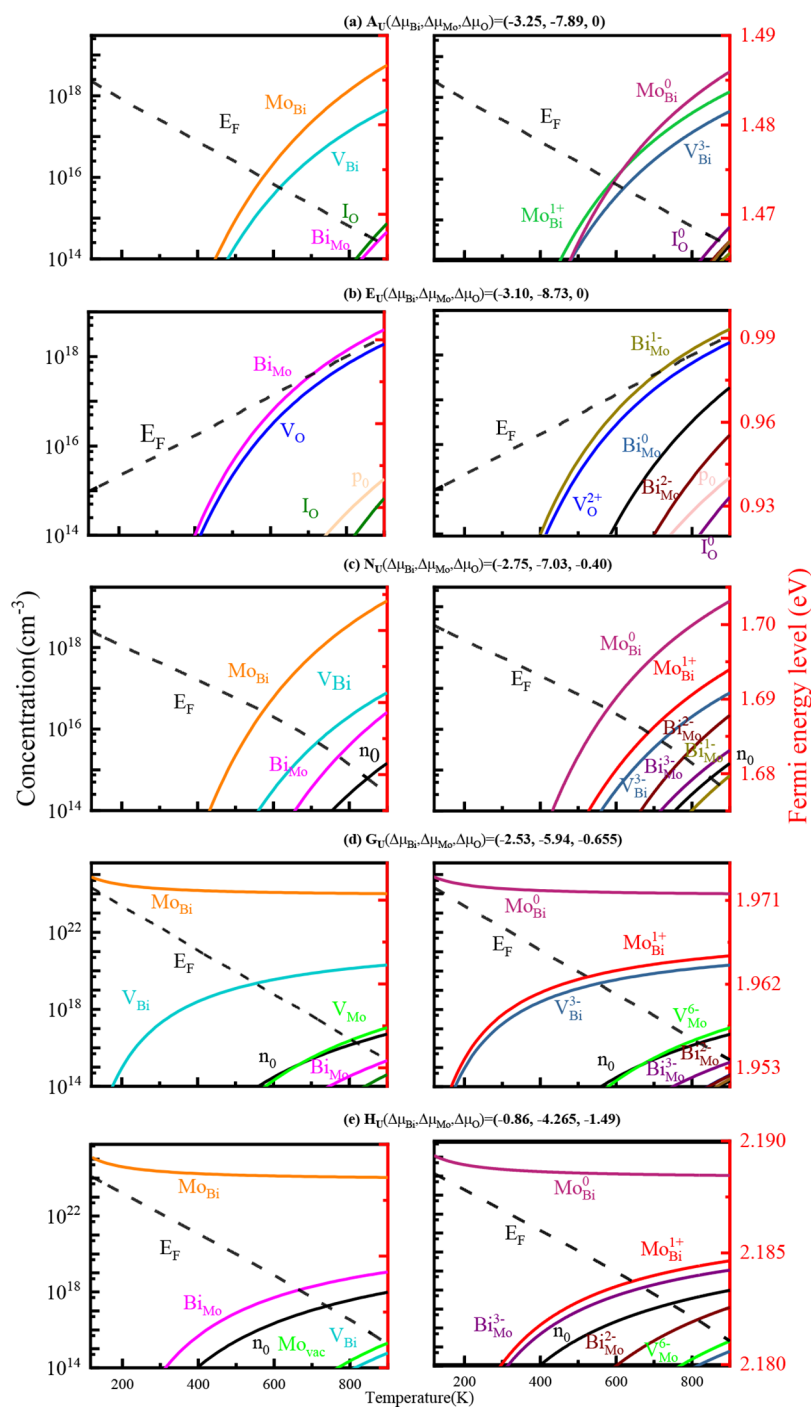
Figure 3. Self-consistent Fermi energy (E_F, black dashed line, right axis) and carrier and defect total concentrations even with mainly charged states (color solid line, left axis) as a function of temperature from 120 to 900 K for intrinsic defects V_{Bi}, V_{Mo}, V_O, I_{Bi}, I_{Mo}, I_O, Mo_{Bi}, and Bi_{Mo} in Bi_2MoO_6 under different chemical potential conditions of (a) A_U, (b) H_U, (c) N_U, (d) G_U, and (e) E_U which derived from PBE + U calculations. The Fermi levels in thermodynamic equilibrium are listed in Table 1.

formation energy of charged defect [eq S1], k is the Boltzmann constant, and T is the temperature. Only defects with adequately low formation energy will be present in large concentrations if the conditions are close to equilibrium, usually in high-temperature growth or annealing.[38] Finally, the condition of charge neutrality in a semiconductor system can be expressed as follows:

$$n_0 - \sum_X \sum_q q[C_X^q] = p_0 \qquad (6)$$

where the sum over all of the acceptor and donors is implicitly included. Since the term of $[Cq\,X]$ in eq 5 depends on a set of defect formation energies $\{E_f(X^q)\}$ varying with T, which come along with the other terms in the equation depending on E_F too. A search algorithm may be used to self-consistently calculate the equilibrium Fermi level positions (E_F), carriers, and defect concentrations satisfying eqs S1 and 1−5 in principle, when given a finite T and certain atomic chemical potentials.

3.3. Temperature Effect. Within the temperature range from 20 to 900 K, the shift of computed self-consistent E_F has

Table 1. Detailed Range of Calculated Fermi Energy Level (eV) in Bi$_2$MoO$_6$ Without/With Doping under Different Chemical Conditions from 120 to 900 K

without/with doping	A_U	E_U	N_U	G_U	H_U
A doping	0.842~1.449	0.658~0.984	0.932~1.580	1.802~1.954	1.807~2.181
only intrinsic defects	1.487~1.466	0.928~0.991	1.702~1.677	1.975~1.954	2.187~2.181
D$^+$ doping	1.699~1.478	1.490~0.998	1.933~1.715	2.029~1.954	2.316~2.182
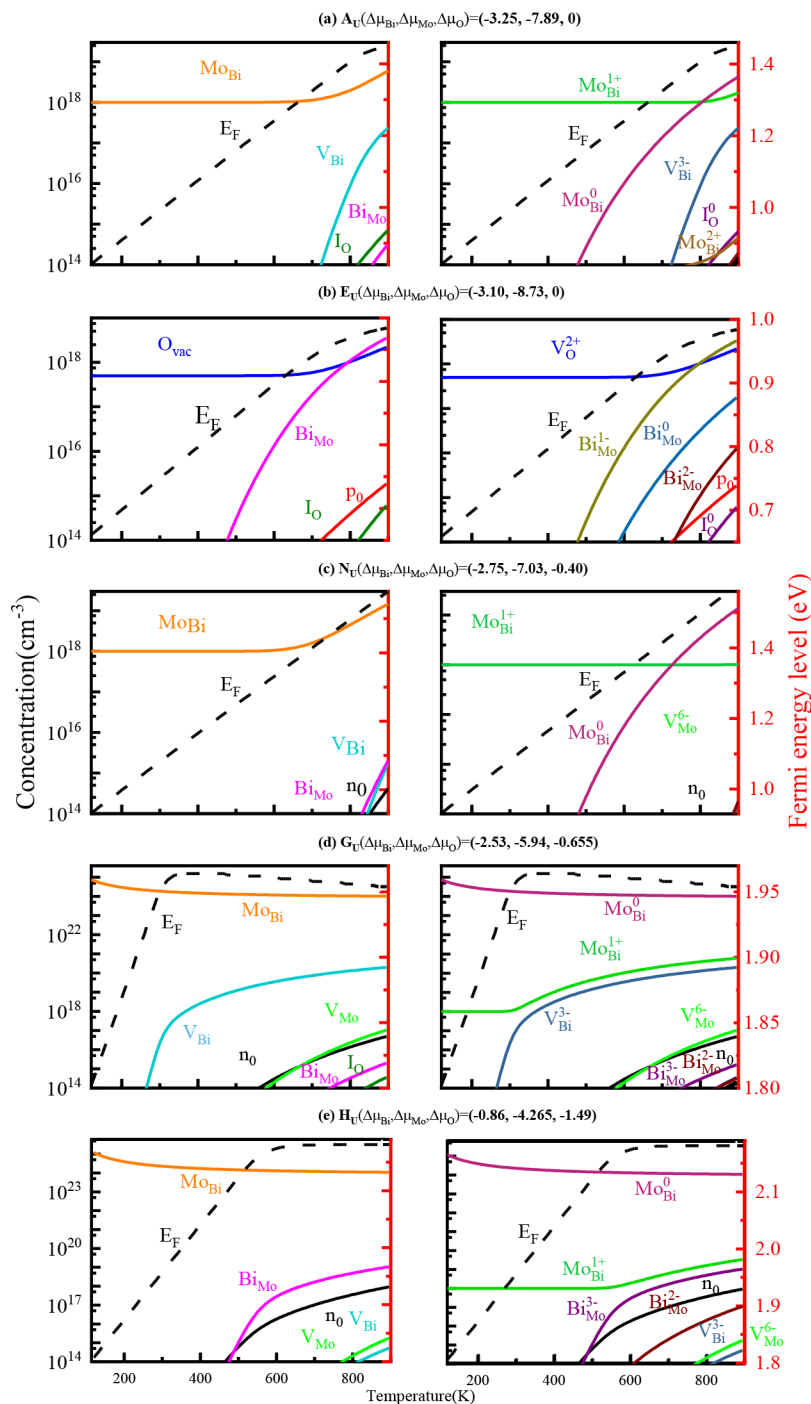
Figure 4. Self-consistent Fermi energy (E_F, black dashed line, right axis) and carrier and defect total concentrations even with mainly charged states (color solid line, left axis) as a function of temperature from 120 to 900 K for intrinsic defect V_{Bi}, V_{Mo}, V_O, I_{Bi}, I_{Mo}, I_O, Mo$_{Bi}$, and Bi$_{Mo}$ in Bi$_2$MoO$_6$ in the presence of a fixed concentration of donors [A$^-$] = 10^{18} cm^{-3} under different chemical potential conditions of (a) A_U, (b) H_U, (c) N_U, (d) G_U, and (e) E_U derived from PBE + U calculations are shown. Fermi levels in thermodynamic equilibrium are listed in Table 1.

been added to the drawing in Figure 2 and listed in Table 1. The same research method also appears in a previous study.[36] The

differences between Fermi-level pinning and the computed self-consistent E_F mainly come from whether the carrier effect is

considered. When variously charged point defects are formed under the constraint of charge neutrality, the self-consistent Fermi levels are further calculated at finite temperatures. They are only tightened in a small area in the band gap, which is marked by an orange-shaded columnar area in Figure 2. It was necessary to note that the concentrations of both defects and their charged states discussed below are all within the strictly constrained and narrow range of the Fermi level. This means the formation energy relationship of defects in the region outside the Fermi level determined by the electric neutral condition will no longer affect the carrier concentration. This provides us with more rigorous and detailed information for the study of defect physics.

At the same time, we found that the lower the formation energy the defects have, the higher the concentration within the range of the calculated Fermi energy level (E_F), and the defect with the lowest formation energy has the highest concentration. However, E_F and all of the defect concentration increases with temperature increase for thermal excitation.[39] At O-rich A_U shown in Figure 3a, the dominant defects are Mo_{Bi}^{1+} and V_{Bi}^{3-} with the typical intrinsic compensation between each other for $T <$ 420 K, and $3[Mo_{Bi}^{1+}] = [V_{Bi}^{3-}]$ holds. When T increases, the concentration of Mo_{Bi}^0 increases without affecting the compensation relationship for its neutral state. Therefore, the calculated Fermi level is near the mid-gap, and n_0 is less than 10^{14} cm^{-3} even at $T = 900$ K. At the same O-rich E_U shown in Figure 3e, Bi_{Mo}^{1-} and V_O^{2+} are the important acceptor and donor defects compensating for each other, and $2[Bi_{Mo}^{1-}]$ is equal to $[V_O^{2+}]$. Moreover, the calculated Fermi level is below the mid-gap, and p_0 is much lower (less than 10^{16} cm^{-3} at 900 K). Therefore, under O-rich conditions (A_U and E_U), the calculated Fermi energy near mid-gap and self-compensation between donors and acceptors would limit its conductivity.[40] The carrier concentration is too low to be used for successful photocatalytic materials.[41] This implied that such extreme O-rich growth conditions should be avoided.

At the moderate points N_U, G_U, and H_U shown in Figure 3b−d, with the lowest formation energy within the range of the calculated Fermi level, the concentration of Bi_{Mo}^0 is higher than that of any other defects. At points N_U and G_U, n_0 are lower than 10^{16} cm^{-3}. Mo_{Bi}^{1+} and V_{Bi}^{3-} are the dominant donors and acceptors with the occurrence of compensation between each other and $3[Mo_{Bi}^{1+}] = [V_{Bi}^{3-}]$ holds, consisting of the situation of O-rich point A_U. At points H_U, the main intrinsic compensation derived from Mo_{Bi}^{1+} and Bi_{Mo}^{3-} with $3[Mo_{Bi}^{1+}] = [Bi_{Mo}^{3-}]$. n_0 is more than 10^{17} cm^{-3} for $T > 700$ K. With $\Delta\mu_O$ decreasing from N_U to G_U to H_U, n_0 increases, suggesting that the growth conditions of nearly O-poor are profitable for its conductivity. This is well agreeable with the universal knowledge.[42,43]

3.4. Doping Effect.
In order to further reveal detailed changes in intrinsic defects concentration and the compensation relationship between intrinsic and extrinsic defects, different chemical growth conditions from 200 to 900 K, E_F, and carrier and defect concentration as a function of temperature are carried out. The results are shown in Figures 4 and 5. They are following the procedure FROZEN-SC-FERMI,[37] in which other charged defects (A$^-$ refers to acceptors with +1 charge state, D$^+$ refers to donors with −1 charge state) of fixed concentration ([A$^-$] = [D$^+$] = 10^{18} cm^{-3}) are introduced, as reported in previous studies.[36,37,44] Remarkably, the calculated Fermi level after doping has also been added in Figure 2 to facilitate comparison with only native defects. It is clear that E_F moves to VBM when the hole concentration increases during acceptor doping and E_F
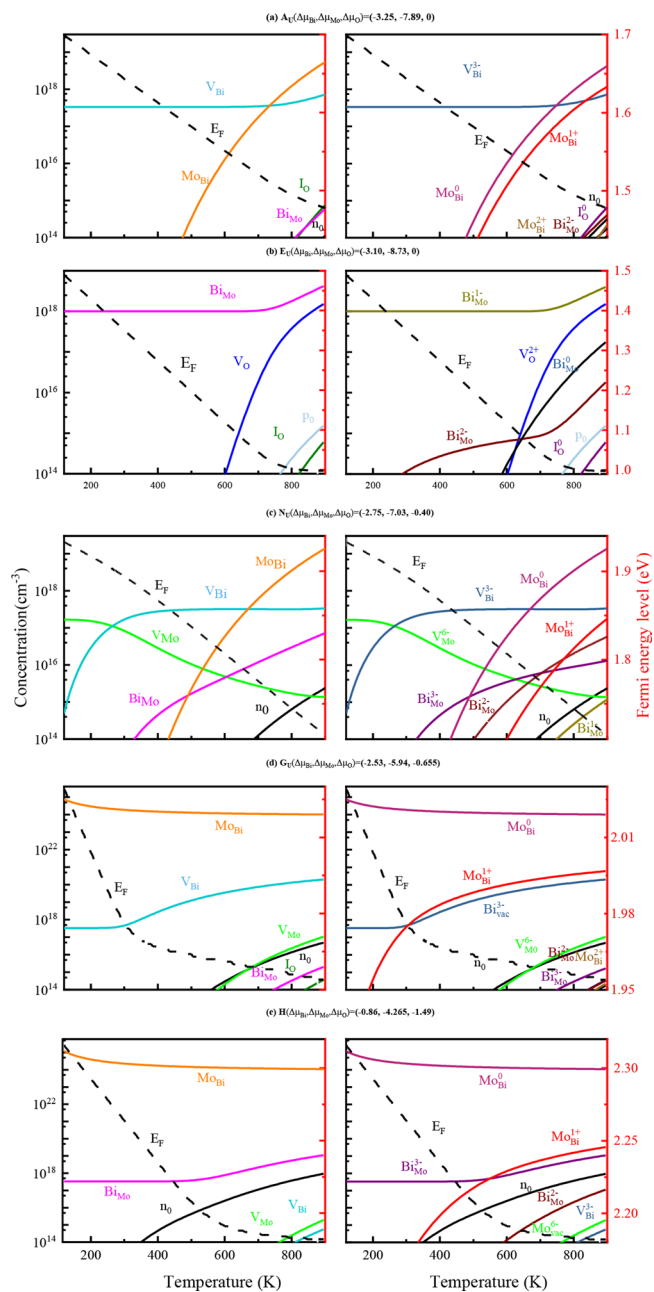
Figure 5. Self-consistent Fermi energy (E_F, black dashed line, right axis) and carrier and defect total concentrations even with mainly charged states (color solid line, left axis) as a function of temperature from 120 to 900 K for intrinsic defects V_{Bi}, V_{Mo}, V_O, I_{Bi}, I_{Mo}, I_O, Mo_{Bi}. and Bi_{Mo} in Bi_2MoO_6 in the presence of a fixed concentration of donors $[D^+] = 10^{18}$ cm^{-3} under different chemical potential conditions of (a) A_U, (b) H_U, (c) N_U, (d) G_U, and (e) E_U derived from PBE + U calculations are shown. The Fermi levels in thermodynamic equilibrium are listed in Table 1.

moves toward CBM when the electron concentration increases during donor doping,[39] as shown by the cyan and blue zones in Figure 2, respectively.

Upon A$^-$ doping from 20 to 900 K, the intrinsic defect concentration is determined by their formation energy relationship in the cyan zone of Figure 2 once more, which is the range of the newly calculated Fermi energy level increasing with T. At O-rich A_U shown in Figure 4a, compensating A$^-$ from 20 to 800 K, Mo_{Bi}^{2+} is the highest concentration defect with the lowest

formation energy in the cyan zone shown in Figure 2a, so $[Mo_{Bi}^{2+}]$ is equal to $[A^-]/2$ for the secondary ionization of Mo_{Bi}. Although the concentration of Mo_{Bi}^0 increases with T increasing, the compensation between Mo_{Bi}^{2+} and A^- is unchanged for the neutral state of Mo_{Bi}^0. Then, as the temperature further increases to above 800 K, $[Mo_{Bi}^{2+}]$ increases above the value necessary to compensate for $[A^-]$ owing to the significant thermal activation of $[V_{Bi}^{3-}]$.[36] At O-rich E_U below 800 K shown in Figure 4e, V_O^{2+} is the highest concentration defect for its lowest formation energy in the cyan zone shown in Figure 2b and compensates A^-, so $[V_O^{2+}] = [A^-]/2$ holds. With T increasing above 800 K, $[V_O^{2+}]$ increases above the value required for compensation $[A^-]$ due to the obvious enhancement of thermal excitation of Bi_{Mo}^{1-}. From the above analysis of intrinsic compensation for A^-, the carrier concentration of the system is less than 10^{16} cm^{-3}. The low efficiency of the A^- doping effect under O-rich conditions is displayed.

At the moderate point, N_U, as shown in Figure 4c, the lowest formation energy is within the cyan zone of the calculated Fermi level, as shown in Figure 2c; Mo_{Bi}^{1+} has the highest concentration, always compensating A^-, so $[Mo_{Bi}^{1+}] = [A^-]$ still holds. At points G_U and H_U shown in Figure 4d,e, Mo_{Bi}^0 with the lowest formation energy within the cyan zone has the highest concentration from 20 to 900 K but has nothing to do with the intrinsic compensation because of its neutral state. At low temperatures, Mo_{Bi}^{1+} compensates A^-, so $[Mo_{Bi}^{1+}]$ is equal to $[A^-]$. At high temperatures, with the thermal excitation of V_{Bi}^{3-} for G_U and Bi_{Mo}^{3-} for H_U increasing, $[Mo_{Bi}^{1+}]$ increases above the value necessary to compensate for $[A^-]$, then $[Mo_{Bi}^{1+}] = ([A^-] + 3[V_{Bi}^{3-}])$ for G_U and $[Mo_{Bi}^{1+}] = ([A^-] + 3[Bi_{Mo}^{3-}])$ for H_U holds. n_0 is more than 10^{16} cm^{-3} for G_U and 10^{17} cm^{-3} for H_U. As $\Delta\mu_O$ decreases from N_U to G_U to H_U, n_0 is slightly lower than that with only intrinsic defects, suggesting that A^- doping is negatively efficient for its conductivity.

After D^+ doping from 20 to 900 K, the E_F zone moves to CBM due to the increase in electron concentration. The intrinsic defect concentration is newly determined by their formation energy relationship in the blue zone, as shown in Figure 2. However, E_F decreases with T increasing because of the increased hole concentration from thermal excitation.[39] At O-rich A_U in Figure 5a, V_{Bi}^{3-} with the lowest formation energy in the blue zone compensates D^+, and $[V_{Bi}^{3-}] = [D^+]/3$ holds. With T increasing, the thermal excitation of Bi_{Mo}^{1-} increases, so $[V_{Bi}^{3-}]$ improves above the value necessary to compensate $[D^+]$ and also compensates $[Bi_{Mo}^{1-}]$ simultaneously to satisfy the charge-neutral condition.

At O-rich E_U in Figure 5b, Bi_{Mo}^{1-} has the lowest formation energy in the blue zone and compensates D^+ for $T < 700$ K with $[Bi_{Mo}^{1-}] = [D^+]$ holding. After that, $[Bi_{Mo}^{1-}]$ increases above the value necessary to compensate $[D^+]$ due to the increase of V_O^{2+} thermal activation. p_0 is more than 10^{16} cm^{-3}, only near 900 K, showing lower conductivity. At the moderate point, N_U is shown in Figure 5c, V_{Mo}^{6-} with the lowest formation energy that compensates D^+ and $[V_{Mo}^{6-}] = [D^+]/6$ holds below 280 K. Then, above 280 K, V_{Bi}^{3-} becomes to compensate D^+ and $[V_{Bi}^{3-}] = [D^+]/3$ holds. The appearance of high compensation of Mo_{Bi}^0 at high temperatures does not affect the compensation relationship and carrier concentration for its neutral charge state. n_0 is less than 10^{16} cm^{-3}, even near 900 K. At the moderate points, H_U and G_U are shown in Figure 5b,d, Mo_{Bi}^0 with the lowest energy in the blue zones in Figure 2d,e has the highest concentration. Bi_{Mo}^{3-} for H_U and V_{Bi}^{3-} for G_U compensate for D^+ at low temperature and increases above the necessary value of compensation for $[D^+]$

due to the increasing thermal activation of with T. With $\Delta\mu_O$ decreasing from N_U to G_U to H_U, n_0 increases and reaches the highest concentration of more than 10^{17} cm^{-3} near 900 K. As $\Delta\mu_O$ decreases from N_U to G_U to H_U, n_0 is slightly higher than that with only intrinsic defects, suggesting that D^+ doping is positively efficient for its conductivity. The O-poor chemical growth conditions are conducive to the conduction of photogenerated carriers.

4. CONCLUSIONS

The formation energy and concentration of intrinsic defects in Bi_2MoO_6 with/without A^- and D^+ doping are explored under different chemical conditions from 120 to 900 K by the GGA + U method. The highest electron concentration is revealed at the relative O-poor point H_U with only intrinsic defects. Moreover, the electron concentration can be further improved after D^+ doping, indicating that the O-poor chemical growth conditions are conducive to photogenerated carriers' conduction. At the same time, we found that the diagram of formation energy vs Fermi level determines the intrinsic defect and carrier concentration under different conditions. During A^-/D^+ doping, E_F moves closer to VBM/CBM for the increasing concentration of holes/electrons. Once the doping conditions are determined, the corresponding E_F is only limited to a small region in the diagram of formation energy vs Fermi level, from which the magnitude relationship of defect concentration can be directly derived from their formation energy. The lower the defect formation energy is, the higher the defect concentration is. The defect with the lowest formation energy has the highest concentration. With E_F moving under different doping conditions, the intrinsic defect concentration changes accordingly. This provides us with a method to adjust the intrinsic defect concentration and deepens our knowledge about comprehension and application of the diagram of formation energy vs Fermi level.

◼ ASSOCIATED CONTENT

Ⓢ Supporting Information

The Supporting Information is available free of charge at https://pubs.acs.org/doi/10.1021/acsomega.3c02161.

DFT and formation energy calculation method; details about the chemical potential calculation (PDF)

◼ AUTHOR INFORMATION

Corresponding Authors

Liming Zhou − *Henan Key Laboratory of Big Data Analysis and Processing, School of Computer and Information Engineering, Henan University, Kaifeng 475001, China*; Email: lmzhou@henu.edu.cn

Wentao Wang − *Guizhou Provincial Key Laboratory of Computational Nano-Material Science, Guizhou Education University, Guiyang 550018, China*; ⊚ orcid.org/0000-0003-4308-3515; Email: wuli8@163.com

Author

Rui Wang − *Henan Key Laboratory of Big Data Analysis and Processing, School of Computer and Information Engineering, Henan University, Kaifeng 475001, China*

Complete contact information is available at:
https://pubs.acs.org/10.1021/acsomega.3c02161

■ REFERENCES

(1) Ran, J.; Zhang, J.; Yu, J.; Jaroniec, M.; Qiao, S. Z. Earth-Abundant Cocatalysts for Semiconductor-Based Photocatalytic Water Splitting. *Chem. Soc. Rev.* **2014**, *43*, 7787−7812.

(2) Chen, C.; Ma, W.; Zhao, J. Semiconductor-Mediated Photo-degradation of Pollutants under Visible-Light Irradiation. *Chem. Soc. Rev.* **2010**, *39*, 4206−4219.

(3) Jiang, J.; Zhao, K.; Xiao, X.; Zhang, L. Synthesis and Facet-Dependent Photoreactivity of BiOCl Single-Crystalline Nanosheets. *J. Am. Chem. Soc.* **2012**, *134*, 4473−4476.

(4) Martínez-de la Cruz, A.; Obregón Alfaro, S.; López Cuéllar, E.; Ortiz Méndez, U. Photocatalytic Properties of Bi_2MoO_6 Nanoparticles Prepared by an Amorphous Complex Precursor. *Catal. Today* **2007**, *129*, 194−199.

(5) Shimodaira, Y.; Kato, H.; Kobayashi, H.; Kudo, A. Photophysical Properties and Photocatalytic Activities of Bismuth Molybdates under Visible light Irradiation. *J. Phys. Chem. B* **2006**, *110*, 17790−17797.

(6) Xiu, Z.; Cao, Y.; Xing, Z.; Zhao, T.; Li, Z.; Zhou, W. Wide Spectral Response Photothermal Catalysis-Fenton Coupling Systems with 3D Hierarchical $Fe_3O_4/Ag/Bi_2MoO_6$ Ternary Hetero-Superstructural Magnetic Microspheres for Efficient High-Toxic Organic Pollutants Removal. *J. Colloid Interface Sci.* **2019**, *533*, 24−33.

(7) Li, H.; Liu, J.; Hou, W.; Du, N.; Zhang, R.; Tao, X. Synthesis and Characterization of $g-C_3N_4/Bi_2MoO_6$ Heterojunctions with Enhanced Visible Light Photocatalytic Activity. *Appl. Catal. B: Environ.* **2014**, *160-161*, 89−97.

(8) Yu, H.; Jiang, L.; Wang, H.; Huang, B.; Yuan, X.; Huang, J.; Zhang, J.; Zeng, G. Modulation of Bi_2MoO_6-Based Materials for Photocatalytic Water Splitting and Environmental Application: A Critical Review. *Small* **2019**, *15*, No. e1901008.

(9) Liu, X.; Gu, S.; Zhao, Y.; Zhou, G.; Li, W. $BiVO_4$, Bi_2WO_6 and Bi_2MoO_6 Photocatalysis: A Brief Review. *J. Mater. Sci. Technol.* **2020**, *56*, 45−68.

(10) Xing, Y.; Zhang, J.; Liu, Z.; Du, C. Steering Photoinduced Charge Kinetics Via Anionic Group Doping in Bi_2MoO_6 for Efficient Photocatalytic Removal of Water Organic Pollutants. *RSC Adv.* **2017**, *7*, 35883−35896.

(11) Wang, D.; Shen, H.; Guo, L.; Wang, C.; Fu, F.; Liang, Y. La and F Co-Doped Bi_2MoO_6 Architectures with Enhanced Photocatalytic Performance Via Synergistic Effect. *RSC Adv.* **2016**, *6*, 71052−71060.

(12) Huang, Z. F.; Pan, L.; Zou, J. J.; Zhang, X.; Wang, L. Nanostructured Bismuth Vanadate-Based Materials for Solar-Energy-Driven Water Oxidation: A Review on Recent Progress. *Nanoscale* **2014**, *6*, 14044−14063.

(13) Jiang, L.; Yuan, X.; Pan, Y.; Liang, J.; Zeng, G.; Wu, Z.; Wang, H. Doping of Graphitic Carbon Nitride for Photocatalysis: A Review. *Appl. Catal. B* **2017**, *217*, 388−406.

(14) Jiang, L.; Yuan, X.; Zeng, G.; Chen, X.; Wu, Z.; Liang, J.; Zhang, J.; Wang, H.; Wang, H. Phosphorus- and Sulfur-Codoped $g-C_3N_4$: Facile Preparation, Mechanism Insight, and Application as Efficient Photocatalyst for Tetracycline and Methyl Orange Degradation under Visible Light Irradiation. *ACS Sustainable Chem. Eng.* **2017**, *5*, 5831−5841.

(15) Song, L. N.; Chen, L.; He, J.; Chen, P.; Zeng, H. K.; Au, C. T.; Yin, S. F. The First Synthesis of Bi Self-Doped $Bi_2MoO_6-Bi_2Mo_3O_{12}$ Composites and Their Excellent Photocatalytic Performance for Selective Oxidation of Aromatic Alkanes under Visible Light Irradiation. *Chem. Commun.* **2017**, *53*, 6480−6483.

(16) Liu, X.; Swihart, M. T. Heavily-Doped Colloidal Semiconductor and Metal Oxide Nanocrystals: An Emerging New Class of Plasmonic Nanomaterials. *Chem. Soc. Rev.* **2014**, *43*, 3908−3920.

(17) Ding, X.; Ho, W.; Shang, J.; Zhang, L. Self Doping Promoted Photocatalytic Removal of No under Visible Light with Bi_2MoO_6: Indispensable Role of Superoxide Ions. *Appl. Catal. B: Environ.* **2016**, *182*, 316−325.

(18) Di, J.; Zhao, X.; Lian, C.; Ji, M.; Xia, J.; Xiong, J.; Zhou, W.; Cao, X.; She, Y.; Liu, H.; Loh, K. P.; Pennycook, S. J.; Li, H.; Liu, Z. Atomically-Thin Bi_2MoO_6 Nanosheets with Vacancy Pairs for Improved Photocatalytic CO_2 Reduction. *Nano Energy* **2019**, *61*, 54−59.

(19) Zhang, L.; Wang, Z.; Hu, C.; Shi, B. Enhanced Photocatalytic Performance by the Synergy of Bi Vacancies and Bi^0 in $Bi_0-Bi_{2-δ}MoO_6$. *Appl. Catal. B: Environ.* **2019**, *257*, No. 117785.

(20) Li, H.; Li, J.; Ai, Z.; Jia, F.; Zhang, L. Oxygen Vacancy-Mediated Photocatalysis of BiOCl: Reactivity, Selectivity, and Perspectives. *Angew. Chem., Int. Ed.* **2018**, *57*, 122−138.

(21) Huang, C.; Ma, S.; Zong, Y.; Gu, J.; Xue, J.; Wang, M. Microwave-Assisted Synthesis of 3D Bi_2MoO_6 Microspheres with Oxygen Vacancies for Enhanced Visible-Light Photocatalytic Activity. *Photochem. Photobiol. Sci.* **2020**, *19*, 1697−1706.

(22) Bai, J.; Li, X.; Hao, Z.; Liu, L. Enhancement of 3D Bi_2MoO_6 Mesoporous Spheres Photocatalytic Performance by Vacancy Engineering. *J. Colloid Interface Sci.* **2020**, *560*, 510−518.

(23) Yang, X.; Wang, S.; Yang, N.; Zhou, W.; Wang, P.; Jiang, K.; Li, S.; Song, H.; Ding, X.; Chen, H.; Ye, J. Oxygen Vacancies Induced Special CO_2 Adsorption Modes on Bi_2MoO_6 for Highly Selective Conversion to CH_4. *Appl. Catal. B: Environ.* **2019**, *259*, No. 118088.

(24) Jing, T.; Dai, Y.; Wei, W.; Ma, X.; Huang, B. Near-Infrared Photocatalytic Activity Induced by Intrinsic Defects in Bi_2MO_6 (M = W, Mo). *Phys. Chem. Chem. Phys.* **2014**, *16*, 18596−18604.

(25) Zhang, J.; Deng, P.; Deng, M.; Shen, H.; Feng, Z.; Li, H. Hybrid Density Functional Theory Study of Native Defects and Nonmetal (C, N, S, and P) Doping in a Bi_2WO_6 Photocatalyst. *ACS Omega* **2020**, *5*, 29081−29091.

(26) Matsubara, M.; Saniz, R.; Partoens, B.; Lamoen, D. Doping Anatase TiO_2 with Group V-b and VI-b Transition Metal Atoms: A Hybrid Functional First-Principles Study. *Phys. Chem. Chem. Phys.* **2017**, *19*, 1945−1952.

(27) Zhang, L.; Man, Y.; Zhu, Y. Effects of Mo Replacement on the Structure and Visible-Light-Induced Photocatalytic Performances of Bi_2WO_6 Photocatalyst. *ACS Catal.* **2011**, *1*, 841−848.

(28) Dudarev, S. L.; Botton, G. A.; Savrasov, S. Y.; Humphreys, C. J.; Sutton, A. P. Electron-Energy-Loss Spectra and the Structural Stability of Nickel Oxide: An LSDA+U Study. *Phys. Rev. B* **1998**, *57*, 1505−1509.

(29) Geneste, G.; Amadon, B.; Torrent, M.; Dezanneau, G. DFT+U Study of Self-Trapping, Trapping, and Mobility of Oxygen-Type Hole Polarons in Barium Stannate. *Phys. Rev. B* **2017**, *96*, No. 134123.

(30) Lany, S.; Zunger, A. Polaronic Hole Localization and Multiple Hole Binding of Acceptors in Oxide Wide-Gap Semiconductors. *Phys. Rev. B* **2009**, *80*, No. 085202.

(31) Gorai, P.; Stevanović, V.; Toberer, E. S. Computationally Guided Discovery of Thermoelectric Materials. *Nat. Rev. Mater.* **2017**, *2*, 17053.

(32) Neugebauer, J.; Van de Walle, C. G. Role of Hydrogen in Doping of GaN. *Appl. Phys. Lett.* **1996**, *68*, 1829−1831.

(33) Yang, J. H.; Yin, W. J.; Park, J. S.; Wei, S. H. Self-Regulation of Charged Defect Compensation and Formation Energy Pinning in Semiconductors. *Sci. Rep.* **2015**, *5*, 16977.

(34) Luo, Z.-F.; Chen, X.-Y.; Lin, S.-Y.; Zhao, Y.-J. Theoretical Study of Structural Stabilities of $BiXO_3$ (X= Cr, Mn, Fe, Ni). *Acta Phys. Sin.* **2013**, *62*, No. 053102.

(35) Zhang, J.; Chen, X.; Deng, M.; Shen, H.; Li, H.; Ding, J. Effects of Native Defects and Cerium Impurity on the Monoclinic $BiVO_4$ Photocatalyst Obtained Via PBE+U Calculations. *Phys. Chem. Chem. Phys.* **2020**, *22*, 25297−25305.

(36) Buckeridge, J.; Veal, T. D.; Catlow, C. R. A.; Scanlon, D. O. Intrinsic Point Defects and the n- and p-type Dopability of the Narrow

Gap Semiconductors GaSb and InSb. *Phys. Rev. B* **2019**, *100*, No. 035207.

(37) Buckeridge, J. Equilibrium Point Defect and Charge Carrier Concentrations in a Material Determined through Calculation of the Self-Consistent Fermi Energy. *Comput. Phys. Commun.* **2019**, *244*, 329−342.

(38) Weston, L.; Bjaalie, L.; Krishnaswamy, K.; Van de Walle, C. G. Origins of n-Type Doping Difficulties in Perovskite Stannates. *Phys. Rev. B* **2018**, *97*, No. 054112.

(39) Yang, J.-H.; Park, J.-S.; Kang, J.; Metzger, W.; Barnes, T.; Wei, S.-H. Tuning the Fermi Level Beyond the Equilibrium Doping Limit through Quenching: The Case of CdTe. *Phys. Rev. B* **2014**, *90*, No. 245202.

(40) Mandel, G. Self-Compensation Limited Conductivity in Binary Semiconductors. I. Theory. *Phys. Rev.* **1964**, *134*, A1073−A1079.

(41) Wang, Z.; Li, J.; Fu, Y. Q. Effective n-Type Doping Strategy through Codoping SiAl−FN in Aluminum Nitride. *Appl. Phys. Express* **2014**, *7*, No. 111004.

(42) Janotti, A.; Varley, J. B.; Rinke, P.; Umezawa, N.; Kresse, G.; Van de Walle, C. G. Hybrid Functional Studies of the Oxygen Vacancy in TiO_2. *Phys. Rev. B* **2010**, *81*, No. 085212.

(43) Nowotny, M. K.; Bak, T.; Nowotny, J. Electrical Properties and Defect Chemistry of TiO_2 Single Crystal. I. Electrical Conductivity. *J. Phys. Chem. B* **2006**, *110*, 16270−16282.

(44) Zhou, Y.; Li, X.; Xi, L.; Yang, J. Intrinsic Defect Study on Ternary ABX_2 Diamond-Like Thermoelectric Materials and Analysis of the Density of Energy Function. *J. Materiomics* **2021**, *7*, 19−24.